AGU PUBLICATIONS

Paleoceanography

RESEARCH ARTICLE
10.1002/2015PA002888

Effects of Drake Passage on a strongly eddying global ocean

Jan P. Viebahn[1], Anna S. von der Heydt[1], Dewi Le Bars[1], and Henk A. Dijkstra[1]

[1] Institute for Marine and Atmospheric Research Utrecht, Utrecht University, Utrecht, Netherlands

Key Points:
- Closing Drake Passage induces significant sea surface warming around Antarctica due to equatorward expansion of the subpolar gyres
- Changing resolution induces quantitative differences related to varying partitions of the subpolar flow into gyres and circumpolar current
- Detailed analyses of the pathways of heat are crucial for a deciphering of mechanisms at work

Correspondence to:
J. P. Viebahn,
J.P.Viebahn@uu.nl

Citation:
Viebahn, J. P., A. S. von der Heydt, D. Le Bars, and H. A. Dijkstra (2016), Effects of Drake Passage on a strongly eddying global ocean, *Paleoceanography*, *31*, 564–581, doi:10.1002/2015PA002888.

Received 14 OCT 2015
Accepted 13 APR 2016
Accepted article online 21 APR 2016
Published online 17 MAY 2016

Abstract The climate impact of ocean gateway openings during the Eocene-Oligocene transition is still under debate. Previous model studies employed grid resolutions at which the impact of mesoscale eddies has to be parameterized. We present results of a state-of-the-art eddy-resolving global ocean model with a closed Drake Passage and compare with results of the same model at noneddying resolution. An analysis of the pathways of heat by decomposing the meridional heat transport into eddy, horizontal, and overturning circulation components indicates that the model behavior on the large scale is qualitatively similar at both resolutions. Closing Drake Passage induces (i) sea surface warming around Antarctica due to equatorward expansion of the subpolar gyres, (ii) the collapse of the overturning circulation related to North Atlantic Deep Water formation leading to surface cooling in the North Atlantic, and (iii) significant equatorward eddy heat transport near Antarctica. However, quantitative details significantly depend on the chosen resolution. The warming around Antarctica is substantially larger for the noneddying configuration (∼5.5°C) than for the eddying configuration (∼2.5°C). This is a consequence of the subpolar mean flow which partitions differently into gyres and circumpolar current at different resolutions. We conclude that for a deciphering of the different mechanisms active in Eocene-Oligocene climate change detailed analyses of the pathways of heat in the different climate subsystems are crucial in order to clearly identify the physical processes actually at work.

1. Introduction

During the past 65 million years (Ma), climate has undergone a major change from a warm and ice-free "greenhouse" to colder "icehouse" conditions with extensive continental ice sheets and polar ice caps [*Katz et al.*, 2008]. The Eocene-Oligocene boundary (∼34 Ma) reflects a major transition and the first clear step into icehouse conditions during the Cenozoic. It is characterized by a rapid expansion of large permanent continental ice sheets on Antarctica which is superimposed on a long-term gradual cooling trend in Cenozoic global climate change [*Zachos et al.*, 2001, 2008].

Proposed mechanisms of the onset of Oligocene glaciation include, on the one hand, increased thermal isolation of Antarctica due to the reorganization of the global ocean circulation induced by critical tectonic opening/widening of ocean gateways surrounding Antarctica [*Kennett*, 1977; *Toggweiler and Bjornsson*, 2000; *Exon et al.*, 2002; *Livermore et al.*, 2007; *Yang et al.*, 2013]. We refer to this perspective as the *ocean gateway mechanism*. On the other hand, declining atmospheric CO_2 concentration from peak levels in the early Eocene has been suggested as a dominant process inducing Antarctic ice sheet growth, the so-called *CO_2 drawdown mechanism* [*DeConto and Pollard*, 2003; *Pagani et al.*, 2011].

Recently, there has been a tendency to discuss these different mechanisms as hypotheses competing against each other [*Goldner et al.*, 2014]. However, a dynamical scenario with several mechanisms at work which can trigger or feedback on each other might ultimately more adequately capture the nonlinearity of climate dynamics [*Livermore et al.*, 2005; *Scher and Martin*, 2006; *Katz et al.*, 2008; *Miller et al.*, 2009; *Sijp et al.*, 2009; *Lefebvre et al.*, 2012; *Dijkstra*, 2013]. Unfortunately, revealing the precise relative roles of different mechanisms active in Cenozoic climate change via comprehensive climate model sensitivity studies is still extremely limited [*Wunsch*, 2010]. Crucial initial and boundary conditions are highly uncertain due to the limited amount of proxy data. In addition, the accurate resolution of the broad range of spatial and temporal scales involved (ranging from fine topographic structures both in the ocean and on Antarctica to the long time scales of continental ice sheet dynamics) exceeds current computational resources.

Correspondingly, the actual physical processes at work within a single mechanism are still under debate [*DeConto et al.*, 2007]. Regarding the ocean gateway mechanism, it is far from clear how the changes in

poleward ocean heat transport are dynamically accomplished [*Huber and Nof*, 2006]. On the one hand, polar cooling has been related to changes in the horizontal gyre circulation with the focus being on either the subtropical western boundary circulation [*Kennett*, 1977; *Exon et al.*, 2002] or the subpolar poleward flow along eastern boundaries [*Huber et al.*, 2004; *Huber and Nof*, 2006; *Sijp et al.*, 2011]. On the other hand, decreased poleward ocean heat transport has been generally attributed to changes in the meridional overturning circulation (MOC) [*Toggweiler and Bjornsson*, 2000; *Sijp and England*, 2004; *Sijp et al.*, 2009; *Cristini et al.*, 2012; *Yang et al.*, 2013]. The MOC, however, can be decomposed into shallow wind-driven gyre overturning cells, deep adiabatic overturning cells (related to North Atlantic Deep Water (NADW) formation), and deep diffusively driven overturning cells (related to bottom waters) [*Kuhlbrodt et al.*, 2007; *Ferrari and Ferreira*, 2011; *Wolfe and Cessi*, 2014]. In other words, the actual pathways of heat and the related physical processes have not been precisely analyzed in previous paleoceanographic model studies (the most extensive studies in this respect are *Huber and Nof* [2006] and *Sijp et al.* [2011]).

Next to the large-scale circulation regimes this also concerns the impact of mesoscale eddies which are known to be of leading-order importance for both the ocean mean state and its response to changing forcing, especially in the Southern Ocean (SO) [*Viebahn and Eden*, 2010; *Hallberg and Gnanadesikan*, 2006; *Munday et al.*, 2015]. For example, interfacial eddy form stresses are crucial in transporting the momentum inserted by the surface wind stress downward to the bottom where they are balanced by bottom form stresses (i.e., the interaction between pressure and topography) [*Munk and Palmen*, 1951; *Olbers et al.*, 2004; *Ward and Hogg*, 2011]. Moreover, interfacial eddy form stresses are equivalent to southward eddy heat fluxes [*Bryden*, 1979], which represent a significant contribution to the total heat flux in specific regions [*Jayne and Marotzke*, 2002; *Meijers et al.*, 2007]. For more details on the crucial role of eddies in both the zonal circulation and the meridional overturning circulation we refer to *Rintoul et al.* [2001] and *Olbers et al.* [2012].

Previous studies on the climatic impact of ocean gateways using general circulation models vary in complexity, including ocean-only, ocean with simple atmosphere, and more recently, coupled ocean-atmosphere models (for an overview see Table 1 in *Yang et al.* [2013]). However, all these models are based on rather coarse ocean model grid resolutions, with the highest horizontal resolution being larger than 2°. As computer power has increased over the past decade, many climate models used for projections of future climate change operate nowadays with a horizontal resolution of about 1° in the ocean component [*Intergovernmental Panel on Climate Change (IPCC)*, 2013]. But even such a resolution is still too coarse to admit mesoscale eddies. Consequently, some version of the Redi neutral diffusion [*Redi*, 1982] and Gent and McWilliams (GM) eddy advection parameterization [*Gent and McWilliams*, 1990] is typically employed in order to represent the effects of mesoscale eddies.

The computational cost of eddy-resolving resolutions is still so high that coupled climate model simulations with resolved eddies have only recently been attempted with relatively short integration times [*McClean et al.*, 2011; *Kirtman et al.*, 2012]. The required huge computational resources eliminate the possibility of multiple control simulations and, hence, the corresponding tuning of model parameters. This also renders the comparison of high-resolution eddy-resolving climate models with low-resolution noneddy-resolving climate models difficult, because the control run climatologies of models at different resolutions are usually quite different. Consequently, investigations of how well coupled climate models using mesoscale eddy parameterizations are able to represent the current climate state as well as the response to changes in climate forcing/boundary conditions are only beginning to emerge [*Bryan et al.*, 2014; *Griffies et al.*, 2015].

For ocean-only models, however, eddy-resolving horizontal resolutions of about 0.1° are nowadays possible even for global-scale simulations. There is no doubt that such a resolution is able to give a much more realistic representation of mesoscale eddies and strong and narrow currents than when coarser resolutions are used [*Farneti et al.*, 2010; *Farneti and Gent*, 2011; *Gent and Danabasoglu*, 2011].

In this study, for the first time, the effects of Drake Passage (DP) in both high-resolution eddy-resolving global ocean model experiments (i.e., nominal 0.1°) and low-resolution noneddy-resolving experiments (i.e., nominal 1°) are compared. In line with many previous studies [*Mikolajewicz et al.*, 1993; *Sijp and England*, 2004; *Sijp et al.*, 2009; *Yang et al.*, 2013], we isolate the influence of DP by closing DP with a land bridge and keeping all other boundary conditions as at present. Of course, such an approach implies two limitations: First, by closing only one gateway, we present a sensitivity study. That is, since we do not employ precise paleogeographic reconstructions [*Baatsen et al.*, 2015], the effects of other gateways (e.g., the Central American Seaway and the Tasman Gateway) are excluded, and hence, we do not model a specific historical paleoclimatic state. Second,

ocean-only models miss the interactions with other crucial components of the climate system, for example, the cryosphere and the carbon cycle. However, sensitivity studies can be insightful because the superposition of multiple feedbacks with additional changes in boundary conditions, such as poorly constrained changes of atmospheric carbon dioxide, can obscure the specific effects of the gateways. In other words, the effects of gateways themselves can be most clearly assessed in relatively simple experiments for which only the gateways are changed while all other boundary conditions are held equal [*Yang et al.*, 2013].

This way our high-resolution ocean-only simulations may serve as a reference for upcoming high-resolution coupled climate model simulations as well as high-resolution simulations based on precise paleogeographic reconstructions. In particular, we employ the ocean component of the Community Earth System Model (CESM) in this study, a climate model that is generally well assessed among the climate models participating in Coupled Model Intercomparison Project Phase 5 [*IPCC*, 2013] and that has already been analyzed in low-resolution paleoconfigurations [*Huber et al.*, 2004; *Huber and Nof*, 2006]. This will allow for comparisons with both previous high-resolution present-day simulations [e.g., *Bryan et al.*, 2014] and future high-resolution paleoclimate simulations employing CESM.

The layout of the paper is as follows: In section 2 we describe the details of the model configuration and the simulations. In sections 3–5 we compare eddying model simulations and noneddying model simulations with both open and closed DP in terms of changes in flow field, sea surface temperature (SST), and meridional heat transport respectively. Section 6 provides a summary and discussion, and we close with conclusions and perspectives in section 7.

2. Model and Simulations

The global ocean model simulations analyzed in this study are performed with the Parallel Ocean Program (POP) [*Dukowicz and Smith*, 1994], developed at Los Alamos National Laboratory. We consider the same two POP configurations as in *Weijer et al.* [2012] and *Den Toom et al.* [2014]. The strongly eddying configuration, indicated by *R*0.1, has a nominal horizontal resolution of 0.1°, which allows the explicit representation of energetic mesoscale features including eddies and boundary currents [*Maltrud et al.*, 2010]. The lower-resolution ("noneddying") configuration of POP, indicated by *x*1, has the nominal 1.0° horizontal resolution. Here "nominal resolution" refers to the fact that the model resolution is not globally fixed but may slightly vary locally, for example, due to grid refinement around the equator or due to a tripolar grid (for details see, e.g., *Maltrud and McClean* [2005]).

The two versions of the model are configured to be consistent with each other, where possible. There are, however, some notable differences, which are discussed in full in the supporting information of *Weijer et al.* [2012]. For the present study we note that the *R*0.1 configuration has a tripolar grid layout, with poles in Canada and Russia, whereas the *x*1 configuration is based on a dipolar grid, with the Northern Pole displaced onto Greenland. In the *R*0.1 configuration, the model has 42 nonequidistant *z* levels, increasing in thickness from 10 m just below the upper boundary to 250 m just above the lower boundary at 6000 m depth. In addition, bottom topography is discretized using partial bottom cells, creating a more accurate and smoother representation of topographic slopes. In contrast, in the *x*1 configuration the bottom is placed at 5500 m depth, there are 40 levels (with the same spacing as in *R*0.1), and the partial bottom cell approach is not used. Finally, in the *x*1 configuration tracer diffusion is accomplished by the GM eddy transport scheme [*Gent and McWilliams*, 1990] using a constant eddy diffusivity of 600 m^2/s (and tapering toward the surface). In summary, the two POP configurations employ different representations of both mesoscale eddies and topographic details which consequently may lead to different interactions between mean flow, mesoscale eddies, and topography [*Adcock and Marshall*, 2000; *Dewar*, 2002; *Barnier et al.*, 2006; *Le Sommer et al.*, 2009].

The atmospheric forcing of the model is based on the repeat annual cycle (normal-year) Coordinated Ocean Reference Experiment (CORE, http://www.clivar.org/organization/wgomd/core) forcing data set [*Large and Yeager*, 2004], with 6-hourly forcing averaged to monthly. Wind stress is computed offline using the Hurrell sea surface temperature (SST) climatology [*Hurrell et al.*, 2008] and standard bulk formulae; evaporation and sensible heat flux were calculated online also using bulk formulae and the model-predicted SST. Precipitation was also taken from the CORE forcing data set. Sea ice cover was prescribed based on the −1.8°C isoline of the SST climatology, with both temperature and salinity restored on a time scale of 30 days under diagnosed climatological sea ice.

As initial condition for the *R*0.1 simulations we use the final state of a 75 years spin-up simulation described in *Maltrud et al.* [2010] using restoring conditions for salinity. The freshwater flux was diagnosed during the last five years of this spin-up simulation, and the simulations we present in this paper use this diagnosed freshwater flux to avoid restoring salinity [see also *Weijer et al.*, 2012; *Den Toom et al.*, 2014]. Using mixed boundary conditions makes the ocean circulation more free to adapt, in particular, to changes in continental geometry [*Sijp and England*, 2004]. For the *x*1 configuration the same procedure as for *R*0.1 is followed except that a more equilibrated initial state is obtained by integrating the model for an additional 500 years under mixed boundary conditions. The *x*1 simulations analyzed in this study then branch off from this state (i.e., end of year 575).

For both configurations, we utilize results of the following two simulations: the unperturbed reference simulation with a present-day bathymetry (DP_{op}) and a simulation in which DP is closed by a land bridge between the Antarctic Peninsula and South America (DP_{cl}). Apart from a closed DP, the DP_{cl} simulations are conducted with the same present-day bathymetry as for the corresponding DP_{op} simulations.

The $DP_{cl}^{R0.1}$ simulation has a duration of 200 years such that the strong adjustment process due to closing DP is largely past. In contrast, the DP_{cl}^{x1} experiment was carried out for a total of 1000 years such that it is closer to a completely equilibrated state. The DP_{op} simulations (having similar durations as the DP_{cl} simulations) are also analyzed in *Weijer et al.* [2012], *Den Toom et al.* [2014], and *Le Bars et al.* [2016], with *Weijer et al.* [2012] presenting a comparison with observations in their supporting information. In this study we use the DP_{op} simulations in order to demonstrate the effects of closing DP. Hence, here we only utilize the DP_{op} simulations in order to define reference states that contrast the DP_{cl} simulations. The analysis of the temporal evolution of the DP_{cl} simulations via Hovmöller diagrams motivates us to mainly use the annual average of the initial year of each DP_{op} simulation as reference states (i.e., year 76 for $DP_{op}^{R0.1}$ and year 576 for DP_{op}^{x1}). We note that quantitative differences which would appear if later years or longer averages are used (i.e., due to low-frequency internal variability or a small trend related to model drift) are small compared to the changes induced by closing DP as far as mean quantities are concerned. For example, variations in the barotropic subpolar circulation of $DP_{op}^{R0.1}$ due to internal variability are in the order of 10 Sverdrup (Sv) [*Le Bars et al.*, 2016], whereas the response to closing DP is in the order of 100 Sv (section 3.1). Regarding eddy quantities, however, the overall magnitude and the response to closing DP are generally smaller (section 5.2) such that internal variability present in $DP^{R0.1}$ induces a dependence on the length of the time averaging period. For that reason we additionally consider multidecadal averages of the initial 20 years of the DP_{op} simulations for the eddy heat transport (section 5.2).

A note of caution regarding our ocean-only model results is necessary. Previous studies [*Zhang et al.*, 1993; *Mikolajewicz and Maier-Reimer*, 1994; *Rahmstorf and Willebrand*, 1995; *Sijp and England*, 2004] have discussed the influence of mixed boundary conditions on the stability of the overturning circulation. In particular, using a restoring boundary condition for temperature implies a model of an atmosphere whose temperature remains fixed or an "infinite heat capacity atmosphere" [*Zhang et al.*, 1993; *Rahmstorf and Willebrand*, 1995]. Applying such an atmospheric model weakens the negative temperature feedback which generally tends to stabilize the overturning related to NADW formation [*Zhang et al.*, 1993; *Mikolajewicz and Maier-Reimer*, 1994]. Obviously, it is up to future studies of high-resolution coupled climate models to ultimately clarify the relative impact of an open/closed DP versus the temperature feedback (as well as the positive salt feedback and the wind feedback) on the stability of the MOC.

3. Flow Field Evolution

For both model configurations *R*0.1 and *x*1 closing DP leads to two major reorganizations of the ocean circulation, namely, the disappearance of the Antarctic Circumpolar Current (ACC) (section 3.1) and the shutdown of NADW formation (section 3.2).

3.1. Barotropic Circulation

Figure 1 shows the annual mean barotropic stream function in the SO for DP_{op}^{x1} (Figure 1a) and $DP_{op}^{R0.1}$ (Figure 1c). The overall large-scale patterns are qualitatively similar and consist of two major regimes: The subtropical flow field (yellow red streamlines) consists of a subtropical gyre within each ocean basin extending to about 40°S, whereas the subpolar flow field (blue magenta streamlines) can be partitioned into the ACC passing through DP and performing large meridional excursions steered by topography [*Rintoul et al.*, 2001; *Olbers et al.*, 2004], and the Weddell and Ross subpolar gyres in the Atlantic basin and Pacific basin, respectively. The

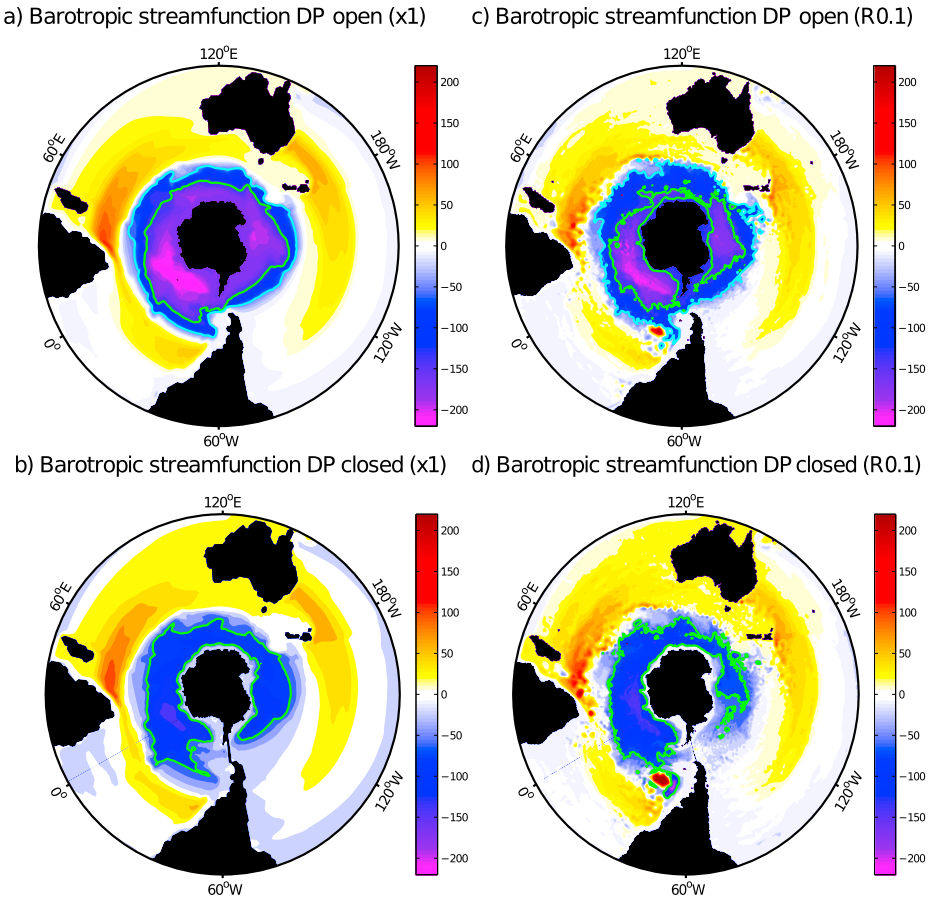

Figure 1. Barotropic stream function (Sv) for low-resolution (a) DP open and (b) DP closed and high-resolution (c) DP open and (d) DP closed. Negative values correspond to clockwise flow. Shown is the annual average of year 576 (Figure 1a), 775 (Figure 1b), 76 (Figure 1c), and 275 (Figure 1d). In Figures 1a and 1c the green (cyan) lines highlight contours of −130 Sv (−50 Sv), whereas in Figures 1b and 1d the green lines highlight contours of −60 Sv.

separating line (i.e., the zero-transport contour) is ultimately determined by the contour of zero wind stress curl [*Pedlosky*, 1996] as well as large-scale topographic steering [*Rintoul et al.*, 2001].

However, the two mean states differ in DP transport (159 Sv for DP_{op}^{x1} and 119 Sv for $DP_{op}^{R0.1}$) as well as maximum westward Weddell gyre transport (−60 Sv for DP_{op}^{x1} and −90 Sv for $DP_{op}^{R0.1}$). That is, the overall stream function minimum (located around 61°S) of the two mean states is similar (about 10 Sv difference), whereas the partitioning of the subpolar flow field into circumpolar current and subpolar gyres is quantitatively substantially different. This is indicated in Figures 1a and 1c by the green lines showing the contours related to −130 Sv for both DP_{op} cases.

Moreover, on top of the large-scale pattern finer eddying structures are present for $DP_{op}^{R0.1}$ (Figure 1c). In the western boundary currents and along strong frontal regions of the ACC mixed barotropic-baroclinic instabilities induce smaller-scale temporal and spatial variability including mesoscale eddies. The most noticeable local features are propagating eddies in the Agulhas Current retroflection region [*Biastoch et al.*, 2008; *Le Bars et al.*, 2014] and the bipolar mode close to Zapiola Rise in the Argentine Basin [*Weijer et al.*, 2007]. We also note that the quantitative details of both the pathway and transport of the circumpolar current depend on interfacial eddy form stresses which transport momentum vertically [*Rintoul et al.*, 2001; *Olbers and Ivchenko*, 2001; *Ward and Hogg*, 2011; *Nadeau and Ferrari*, 2015] as well as on the topographic details which are part (via eddy-mean flow and topography interactions) of the ultimate balance between input of momentum by surface winds and bottom form stress [*Olbers et al.*, 2004; *Hogg and Munday*, 2014; *Munday et al.*, 2015].

Figure 1 also shows the annual mean barotropic stream function in the SO for DP_{cl}^{x1} (Figure 1b) and $DP_{cl}^{R0.1}$ (Figure 1d). Again, the overall large-scale circulation patterns are similar. The zero-transport contour which

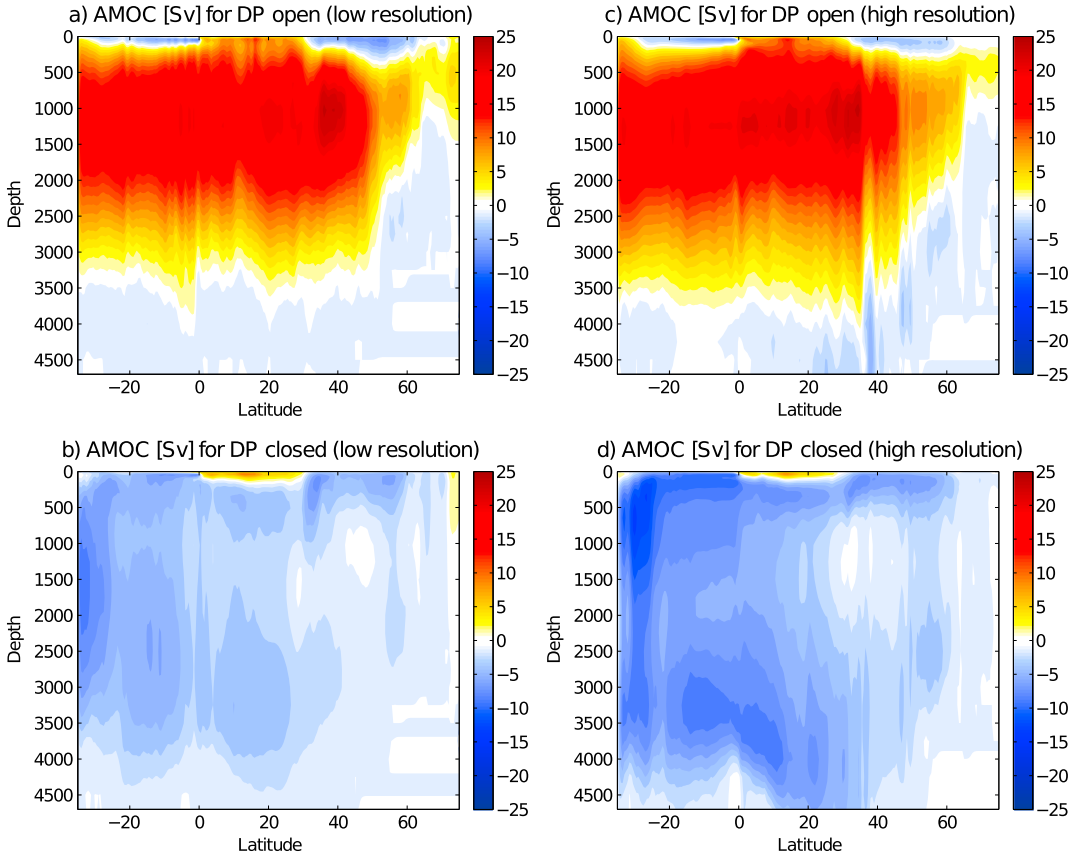

Figure 2. Atlantic meridional overturning stream function (Sv) for low-resolution (a) DP open and (b) DP closed and high-resolution (c) DP open and (d) DP closed. Shown is the annual average of year 576 (Figure 2a), 775 (Figure 2b), 76 (Figure 2c), and 275 (Figure 2d).

separates the subtropical and subpolar flow fields is roughly the same as for the DP_{op} cases due to the fixed wind stress curl and the apart from DP unchanged topography. Consequently, in the absence of a circumpolar flow the subpolar gyres expand equatorward and now entirely occupy the (largely unchanged) physical space of the subpolar flow field. In terms of the adjustment process the former ACC transport is mostly included into the subpolar gyre system such that the westward subpolar gyre transports drastically increase. For example, for both configurations ($x1$ and $R0.1$) the westward Weddell gyre transport initially increases to about 200 Sv, which subsequently reduces to about 150 Sv during the adjustment process (not shown) such that the overall stream function minimum in Figures 1b and 1d is smaller compared to the corresponding DP_{op} cases (Figures 1a and 1c). The green lines in Figures 1b and 1d show the contours related to −60 Sv and indicate the overall similarity of the subpolar flow fields of DP_{cl}^{x1} and $DP_{cl}^{R0.1}$. On the other hand, the large-scale subtropical gyre system remains relatively unaffected by closing DP (for both $x1$ and $R0.1$) with only a small part of the former ACC transport entering it (the Indonesian throughflow and Mozambique Current transports increase by about 5 Sv).

Consequently, the differences between the configurations $x1$ and $R0.1$ in the mean barotropic circulation appear to be less drastic for DP_{cl} (Figures 1b and 1d) than for DP_{op} (Figures 1a and 1c). Of course, the explicit representation of mesoscale instabilities in $DP_{cl}^{R0.1}$ (Figure 1d) induces smaller-scale spatial and temporal variability which is not present in DP_{cl}^{x1} (Figure 1b). But closing DP suspends the issue of the partitioning of the subpolar flow field into circumpolar flow and subpolar gyres. This makes the flow dynamics less intricate and potentially less prone to differences in resolution.

3.2. Meridional Overturning Circulation

Figure 2 shows the annual mean Atlantic MOC (AMOC) for all model simulations. The AMOC patterns of DP_{op}^{x1} (Figure 2a) and $DP_{op}^{R0.1}$ (Figure 2c) are very similar to each other [see also *Weijer et al.*, 2012]. They exhibit the typical present-day Atlantic upper overturning cell with northward flow near the surface (interlooped with

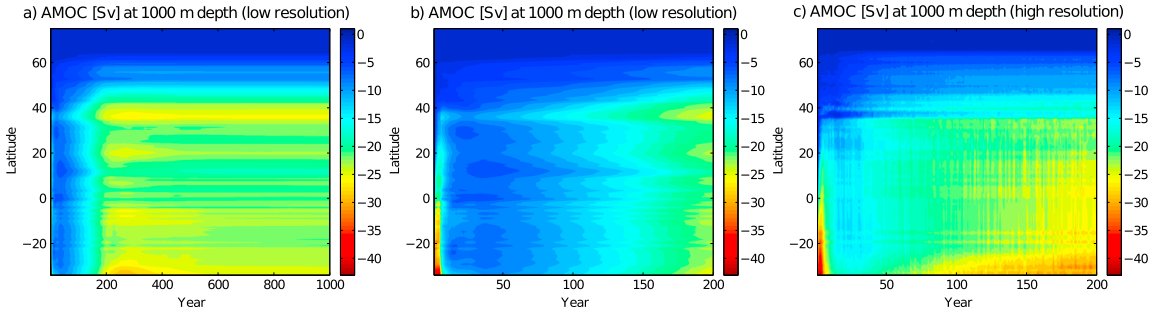

Figure 3. Hovmöller diagram of the annual mean Atlantic meridional overturning circulation (Sv) at 1000 m depth for DP closed and (a and b) low resolution (showing the entire 1000 years and the first 200 years of the simulation), (c) high resolution. Values are relative to the corresponding annual average for DP open at reference year 576 (Figures 3a and 3b) and reference year 76 (Figure 3c).

shallow-gyre overturning cells), NADW formation in the subpolar regions (seas surrounding Greenland), and southward flow at middepth (along the western boundary of the Atlantic Ocean). For DP^{x1}_{op} ($DP^{R0.1}_{op}$) the maximum of the AMOC is 24.0 Sv (24.1 Sv) and centered at 36°N (34.5°N) and about 1000 m depth. The deep overturning cell related to Antarctic Bottom Water is very weak.

In contrast, for both DP^{x1}_{cl} (Figure 2b) and $DP^{R0.1}_{cl}$ (Figure 2d) the NADW formation shuts down, and the deep AMOC is dominated by counterclockwise overturning cells. For DP^{x1}_{cl} ($DP^{R0.1}_{cl}$) the overturning magnitude is about −8.5 Sv (−12.9 Sv) and centered at 34°S (30°S) and about 1500 m (650 m) depth. But, of course, the precise structure and magnitude of the deep counterclockwise overturning cells surely still need several hundreds of years more in order to completely equilibrate at all depths.

However, Figure 3 shows Hovmöller diagrams of the AMOC at around 1000 m depth for both DP^{x1}_{cl} (Figures 3a and 3b) and $DP^{R0.1}_{cl}$ (Figure 3c). The Hovmöller diagrams indicate that the temporal evolution of the shut down of NADW formation is very similar for both resolutions with $DP^{R0.1}_{cl}$ evolving slightly faster than DP^{x1}_{cl}. That is, within the first 5–10 years a drastic decrease in AMOC occurs (up to 40 Sv in the South Atlantic) for both $DP^{R0.1}_{cl}$ (Figure 3c) and DP^{x1}_{cl} (Figure 3b). Subsequently, the AMOC partially recovers for a period of 20–40 years, whereupon it again decreases to reach its near-equilibrium values. Note that at the end of the simulation the AMOC at around 1000 m depth and 26°N in DP^{x1}_{cl} ($DP^{R0.1}_{cl}$) has a drift of −0.002 Sv (−0.05 Sv) per decade.

4. Sea Surface Temperature Evolution

Figure 4 shows the changes in SST due to closing DP for both configurations *x*1 (Figures 4a and 4b) and *R*0.1 (Figures 4c and 4d). The overall large-scale pattern of SST change is similar for both model resolutions (compare Figures 4a and 4c). The largest increase in SST is located at the Antarctic coast west of DP where subpolar gyre streamlines bend from near-subtropical latitudes toward Antarctica. From there the increase in SST gradually diminishes both in the zonal and the meridional directions.

The Hovmöller diagrams (Figures 4b and 4d) indicate that for both configurations *x*1 and *R*0.1 most of this SST increase occurs within the very first years with only smaller adjustments on longer time scales. However, the magnitude of the increase in SST around Antarctica is significantly larger for *x*1 than for *R*0.1. For example, the increase in zonal mean SST at 70°S is about 5.5°C for DP^{x1}_{cl} and about 2.5°C for $DP^{R0.1}_{cl}$ (with the zonal mean SSTs of DP^{x1}_{op} and $DP^{R0.1}_{op}$ being essentially identical). In section 5.3 we demonstrate that this difference in SST change between the two model resolutions is related to the difference in partitioning of the subpolar flow into circumpolar current and gyres (see also section 3.1).

A second local maximum in SST change occurs at a latitude band around 40°S (see Figures 4a and 4c). For both model resolutions a hot spot of warming is located near the Agulhas retroflection region. However, in the *R*0.1 configuration another hot spot appears in the Argentine Basin which is much less pronounced for the *x*1 configuration. This local feature is related to the bipolar mode close to Zapiola Rise [*Weijer et al.*, 2007] and, hence, genuinely related to smaller-scale spatial variability which is not captured by the model grid resolution of *x*1 (and the GM parameterization).

Finally, we notice that the SST in the (sub)tropics between 35°S and 35°N remains largely unaffected, whereas significant cooling occurs in the North Atlantic (see Figures 4b and 4d). The maximum cooling in zonal mean

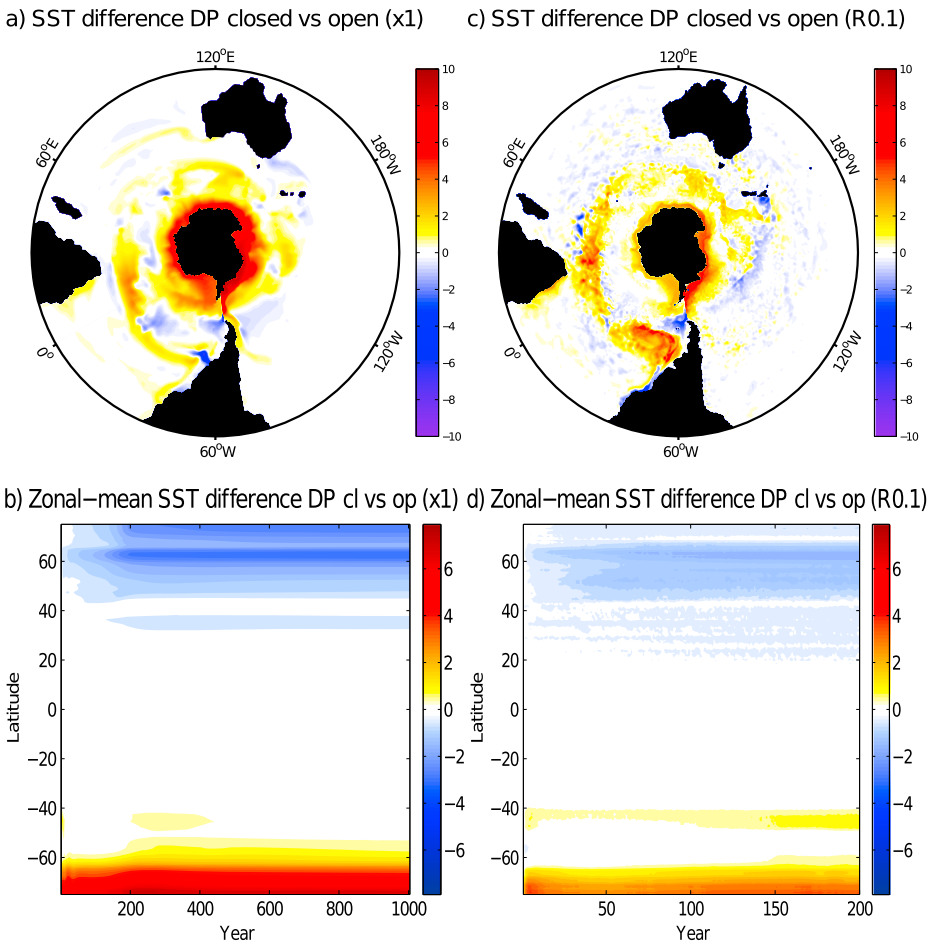

Figure 4. Annual mean SST difference (°C) between DP closed and reference year of DP open for (a and b) low resolution (reference year is 576) and (c and d) high resolution (reference year is 76). For DP closed the years 775 (Figure 4a) and 275 (Figure 4c) are shown. Figures 4b and 4d show Hovmöller diagrams of the zonal mean SST.

SST is located around 60°N (i.e., the Nordic Seas surrounding Greenland) and is about 2.0°C (1.3° C) for *x*1 (*R*0.1). The temporal evolution of this SST decrease occurs on a longer time scale compared to the warming around Antarctica and is mainly related to the shutdown of the overturning cell related to NADW formation (see also section 5.3).

5. Meridional Heat Transport

The ocean potential temperature *T* is linked to the ocean flow field via the ocean heat budget. The ocean heat budget relates the time tendency of *T* (i.e., ocean heat content) to both the divergence of heat transport by the ocean flow field and the surface heat fluxes [*Griffies et al.*, 2015; *Yang et al.*, 2015]. Within the longitude and depth integrated heat budget the ocean flow field predominantly enters via the advective meridional heat transport,

$$\mathrm{MHT} \equiv C_p \rho_0 \iint vT \, \mathrm{d}x\mathrm{d}z \,, \tag{1}$$

where *v* represents the meridional velocity (also including the GM part for *x*1), ρ_0 the reference density, and C_p the ocean heat capacity. That is, if there is no regional storage of heat within the ocean and contributions to the meridional heat transport by subgrid-scale processes (e.g., diffusion) are small, then the air-sea heat fluxes are balanced by the meridional divergence of MHT at each latitude.

5.1. Global and Basin-Wide Depth Integrated Heat Advection

Figure 5 displays the annual mean MHT for the global ocean (Figure 5a) as well as its decomposition into Atlantic-Arctic (AA, Figure 5c) and Indo-Pacific (IP, Figure 5d) components. For the control simulations $\mathrm{DP}_{\mathrm{op}}^{R0.1}$

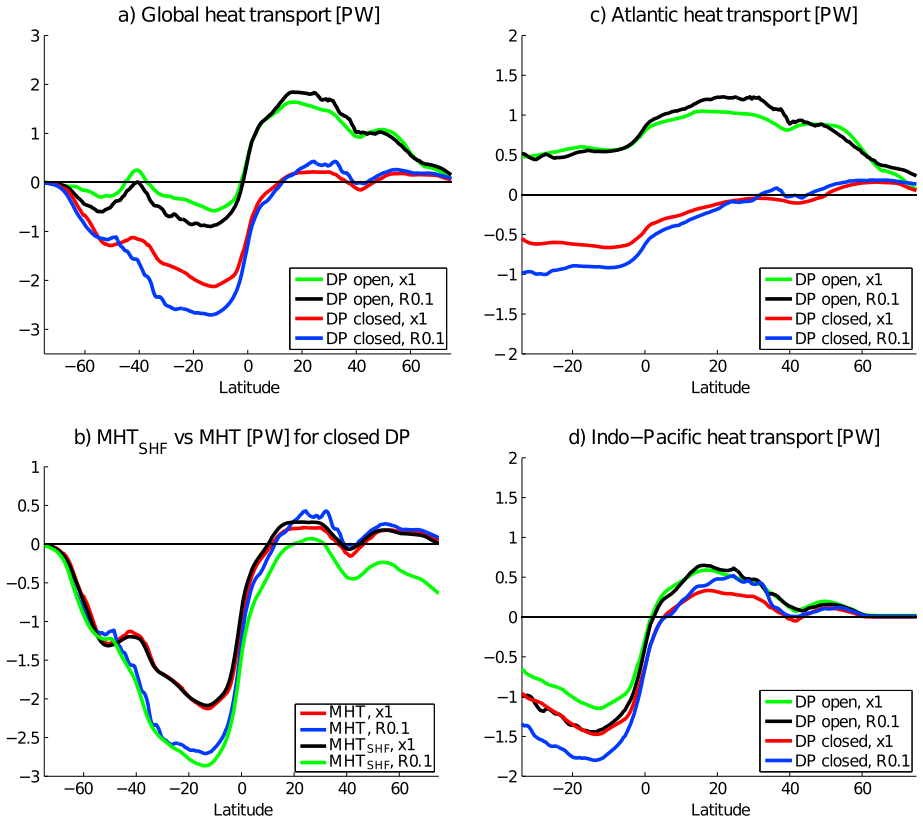

Figure 5. The (a) global, (c) Atlantic-Arctic, and (d) Indo-Pacific annual-mean advective meridional heat transports (PW) for all model simulations are shown. For the control simulations the reference years 76 (for $DP_{op}^{R0.1}$) and 576 (for DP_{op}^{x1}) are presented (the curves remain essentially unchanged for later years). For the closed DP simulations the years 275 (for $DP_{cl}^{R0.1}$) and 1575 (for DP_{cl}^{x1}) are shown. Also, (b) the zonally and meridionally integrated (from south to north) surface heat flux (MHT_{SHF}) is drawn for the closed DP simulations. For comparison the corresponding global advective meridional heat transport is shown again (same as in Figure 5a).

(black curve) and DP_{op}^{x1} (green curve) the overall behavior is very similar exhibiting the present-day structure of a hemispherically antisymmetric distribution in the IP (i.e., MHT from the equator to the poles which is slightly larger in the Southern Hemisphere (SH) due to the addition of the Indian Ocean) but northward MHT in the entire AA (due to the overturning circulation related to NADW formation). Consequently, the global MHT from the equator to the poles is significantly larger in the Northern Hemisphere (NH) than in the SH with the local minimum around 40°S (related to the boundary between subtropical gyres and ACC) even showing small equatorward transport. The main difference between $DP_{op}^{R0.1}$ and DP_{op}^{x1} is that the magnitude of MHT is slightly larger in $DP_{op}^{R0.1}$ than in DP_{op}^{x1}, as it is found in other recent studies comparing the MHT of low-resolution and high-resolution present-day climate model simulations [*Bryan et al.*, 2014; *Griffies et al.*, 2015]. More precisely, for $DP_{op}^{R0.1}$ (DP_{op}^{x1}) the maximum global/AA/IP MHT is 1.85/1.23/0.65 PW (1.64/1.05/0.59 PW), and the minimum global/IP MHT is −0.9/−1.44 PW (−0.58/−1.15 PW). That is, in the NH the smaller MHT of DP_{op}^{x1} is mostly located in the Atlantic, whereas in (sub)tropics of the SH smaller MHT is mainly present in the IP. However, most crucial for this study is that in the SO (i.e., south of 35°S) the MHT of DP_{op}^{x1} is smaller as well (Figure 5a).

Figure 5 also shows the corresponding annual mean MHT for both $DP_{cl}^{R0.1}$ (blue curve) and DP_{cl}^{x1} (red curve) with again very similar overall behavior for both resolutions. The magnitude of the global MHT (Figure 5a) is drastically reduced in the NH and drastically increased in the SH leading to the reversed distribution of DP_{op}. That is, the global MHT from the equator to the poles is significantly larger in the SH than in the NH with the local minimum around 40°N (related to the boundary between subtropical and subpolar gyres) even showing small equatorward transport. The maximum change is of about 2 PW and is mostly located in the AA (maximum change of about 1.5 PW, Figure 5c) where the MHT turns into southward MHT within the entire (sub)tropics (35°S<y<35°N). The IP (Figure 5d) keeps a hemispherically antisymmetric distribution (MHT from the equator to the poles), but the magnitude of MHT is increased in the SH (up to 0.5 PW) and decreased in

the NH. Again, the main difference between the two configurations is that the maximum values in $DP_{cl}^{R0.1}$ are generally larger compared to DP_{cl}^{x1}. However, we observe that within the SO the difference in MHT between the configurations is significantly reduced with nearly identical values south of 50°S (Figure 5a).

Regarding the adjustment processes that are still active in the DP closed simulations, we note that the air-sea heat fluxes can be integrated meridionally to obtain an estimate of MHT necessary to balance the loss or gain of heat through air-sea exchange. Observational estimates of the meridional heat transport are typically based on this indirect calculation via air-sea heat fluxes [*Macdonald and Baringer*, 2013]. Within numerical ocean models the comparison of direct and indirect meridional heat transport computations gives an indication of the equilibration of the ocean state and whether fundamental physical constraints like mass and energy conservation are satisfied [*Yang et al.*, 2015]. Figure 5b shows both the zonally and meridionally integrated (from south to north) surface heat flux (indicated by MHT_{SHF}) and the global MHT (same as in 5a) for both $DP_{cl}^{R0.1}$ and DP_{cl}^{x1}. For DP_{cl}^{x1} the MHT and MHT_{SHF} nearly overlap which demonstrates that the ocean heat content is largely equilibrated at every latitude. For $DP_{cl}^{R0.1}$, on the other hand, the ocean heat content is still slightly adjusting within subtropics of the SH as well as more substantially within the NH. Nevertheless, south of 50°S the MHT and MHT_{SHF} almost perfectly overlap. This indicates that the SO is the region where the ocean heat content reaches a near-equilibrium state first, in correspondence with the Hovmöller diagrams of SST (Figures 4b and 4d). Regarding the model equilibration in a 3-D sense, we also note for completeness that the surface warming within the SO due to closing DP (discussed in section 4) extends to about 1000 m depth. At depths of around 1500–4000 m DP_{cl}^{x1} ($DP_{cl}^{R0.1}$) shows cooling in the SO with a remaining drift of −0.003°C (−0.028°C) per decade at the end of the simulation (not shown).

However, crucial questions remain: What are the respective roles of the mean flow and the eddy field in the MHT for the simulations DP_{op} and DP_{cl}? What are the respective contributions of the barotropic circulation (section 3.1) and the overturning circulation (section 3.2) to the corresponding (changes in) MHT? Do the two configurations *R*0.1 and *x*1 behave differently in these respects? In previous paleoceanographic gateway studies these attribution questions (i.e., the partitioning of MHT into different dynamical components) were not or only loosely addressed. But in order to understand changes in MHT, it is mandatory to determine what physical processes control the MHT [*Ferrari and Ferreira*, 2011]. In order to relate the (changes in) MHT more precisely to individual contributions of different physical processes, we perform both temporal and spatial decompositions of the global MHT in the following two sections.

5.2. Temporal Decomposition of the Depth Integrated Heat Advection

We decompose the global MHT into a time mean component,

$$\overline{\mathrm{MHT}} \equiv C_p \rho_0 \iint \overline{v}^t \overline{T}^t \, \mathrm{d}x\mathrm{d}z \,, \tag{2}$$

and a transient eddy component (also including the GM part for *x*1),

$$\mathrm{MHT}' \equiv C_p \rho_0 \iint \overline{vT}^t - \overline{v}^t \overline{T}^t \, \mathrm{d}x\mathrm{d}z \,, \tag{3}$$

based on the temporal mean $\overline{\cdot}^t$. We note that the variability within the noneddying configuration (*x*1) is essentially given by the seasonal cycle, whereas within the eddying configuration (*R*0.1) also internal variability on interannual to decadal time scales is present [*Le Bars et al.*, 2016]. Consequently, the eddy mean decomposition of the eddying configuration partly depends on the chosen length of the time averaging period. Different averaging intervals affect mostly MHT′ due to its relatively small magnitudes, whereas MHT and $\overline{\mathrm{MHT}}$ remain largely unchanged. For that reason we discuss MHT′ with respect to both 1 year and 20 year average periods in the following.

Figure 6a shows the annual mean $\overline{\mathrm{MHT}}$ for all simulations. In each case $\overline{\mathrm{MHT}}$ follows largely the corresponding MHT (compare with Figure 5a) such that the overall similarity between $\overline{\mathrm{MHT}}$ and MHT typically found for DP_{op} [*Bryan et al.*, 2014; *Griffies et al.*, 2015; *Yang et al.*, 2015] equally holds for DP_{cl}. In particular, similar to MHT we find that the magnitudes of $\overline{\mathrm{MHT}}$ are generally larger for the eddying configuration but that south of 50°S both $DP_{cl}^{R0.1}$ and DP_{cl}^{x1} show nearly identical values (in contrast to DP_{op}).

The difference between MHT and $\overline{\mathrm{MHT}}$, i.e., MHT′, is shown in Figure 7 for both annual (Figure 7a) and multidecadal (Figure 7b) averaging periods. Focussing on DP_{op}^{x1} (green line, essentially unaffected by the averaging

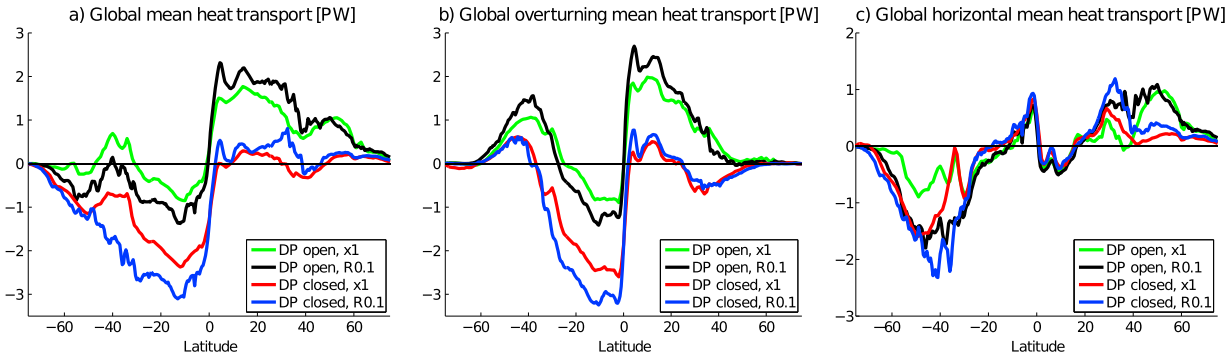

Figure 6. The (a) time mean component of the global advective meridional heat transport (PW) and its decomposition into components related to (b) meridional overturning circulations and (c) horizontal circulations are shown for all simulations. The annual averages are performed for the same years as in Figure 5.

period) we find the structure of MHT′ typically described in previous studies using decadal averaging periods [*Bryan*, 1996; *Jayne and Marotzke*, 2002; *Volkov et al.*, 2008; *Bryan et al.*, 2014; *Griffies et al.*, 2015]. Significant magnitudes of MHT′ (i.e., in the order of $\overline{\mathrm{MHT}}$) are found in three main regions: a strong convergence of MHT′ opposing $\overline{\mathrm{MHT}}$ is found in the tropics and related to tropical instability waves; additionally, around 35°S and 35°N peaks of poleward MHT′ are present and related to western boundary currents (e.g., the Kuroshio Current or the Brazil-Malvinas Confluence regions) as well as their extensions into the ocean interior (i.e., eddy-induced heat transport across gyre boundaries), the Agulhas Retroflection and the ACC.

The MHT′ of $\mathrm{DP}_{\mathrm{cl}}^{x1}$ exhibits exactly the same structure (compare red and green lines) with slightly smaller values in the tropics and around 35°N and slightly larger values around 35°S. This largely insensitive behavior may indicate that the MHT′ is dominated by wind-driven instabilities which are largely determined by the prescribed wind stress. One exception occurs south of 60°S where the nearly vanishing southward MHT′ of $\mathrm{DP}_{\mathrm{op}}^{x1}$ turns into a substantial northward MHT′ for $\mathrm{DP}_{\mathrm{cl}}^{x1}$ (red line). This eddy transport is induced by the intensification of the subpolar gyre Antarctic boundary current due to the integration of the former ACC into the subpolar gyre system.

The MHT′s of both $\mathrm{DP}_{\mathrm{op}}^{R0.1}$ (black line) and $\mathrm{DP}_{\mathrm{cl}}^{R0.1}$ (blue line) related to multidecadal averages (Figure 7b) show a similar structure as the corresponding MHT′ of the noneddying simulations. In particular, for a closed DP the MHT′ decreases in the tropics and NH, whereas it slightly increases around 40°S and a substantial northward MHT′ emerges near Antarctica. Compared to DP^{x1} the magnitudes are larger in the tropics but smaller south of 20°S. North of 20°N, the magnitudes are also smaller except for the strong peak around 40°N. These quantitative differences are largely related to the different pathways of western boundary current extensions for different resolutions [*Griffies et al.*, 2015].

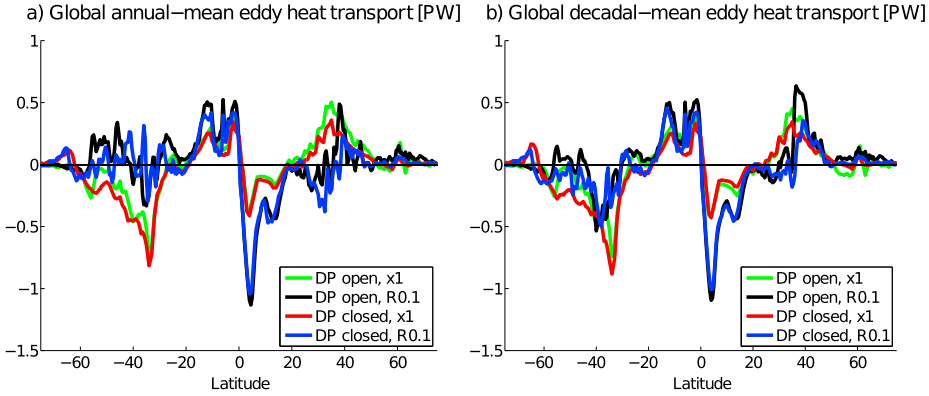

Figure 7. The eddy component of the global advective meridional heat transport (PW) is shown for all simulations and two averaging intervals. (a) Annual averages are used for the same years as in Figure 5. (b) The 20 year averages are performed of years 76–95 (for $\mathrm{DP}_{\mathrm{op}}^{R0.1}$), 576–595 (for $\mathrm{DP}_{\mathrm{op}}^{x1}$), 256–275 (for $\mathrm{DP}_{\mathrm{cl}}^{R0.1}$), and 756–775 (for $\mathrm{DP}_{\mathrm{cl}}^{x1}$).

Finally, Figure 7a also shows the MHT′s of both $DP_{op}^{R0.1}$ (black line) and $DP_{cl}^{R0.1}$ (blue line) for annual averages. Within the tropics and south of 60°S (as well as north of 50°N) the MHT′ is largely unaffected by the time-averaging period. However, in between these regions significant differences appear with MHT′ having smaller magnitudes and partly turning from poleward to equatorward. These differences are related to interannual variability and show that the MHT′ of the noneddying simulations (based on the GM parameterization) gives an adequate representation of the MHT′ of the eddying simulations generally only in a decadal mean sense (Figure 7b). Nevertheless, the low-resolution MHT′ is able to capture the qualitative changes south of 60°S for both averaging intervals in our simulations.

In summary, closing DP induces only relatively small quantitative changes in the MHT′. The only qualitative change is the emergence of northward transport south of 60°S which is well captured by the noneddying simulation too. Consequently, the changes in MHT (Figure 5a) due to a closed DP are dominated by the changes in $\overline{\mathrm{MHT}}$ (Figure 6a). For that reason we decompose $\overline{\mathrm{MHT}}$ in the following section in order to relate the circulation changes described in section 3 to the changes in MHT.

5.3. Spatial Decomposition of the Time Mean Depth Integrated Heat Advection

We decompose the global $\overline{\mathrm{MHT}}$ based on the global zonal mean $\bar{\cdot}^{x}$ into a component related to time mean meridional overturning circulations,

$$\overline{\mathrm{MHT}}_O \equiv C_p \rho_0 \iint \bar{v}^{tx} \bar{T}^{t} \, \mathrm{d}x\mathrm{d}z \,, \tag{4}$$

and a component related to time mean horizontal circulations,

$$\overline{\mathrm{MHT}}_H \equiv C_p \rho_0 \iint (\bar{v}^{t} - \bar{v}^{tx}) \bar{T}^{t} \, \mathrm{d}x\mathrm{d}z \,, \tag{5}$$

as introduced by *Hall and Bryden* [1982] [see also *Bryden and Imawaki*, 2001; *Macdonald and Baringer*, 2013] and applied to the SO, e.g., by *Treguier et al.* [2007] and *Volkov et al.* [2010]. In other contexts $\overline{\mathrm{MHT}}_H$ is also referred to as the standing eddy heat transport [*Marshall et al.*, 1993; *Viebahn and Eden*, 2012].

We note that this decomposition does not entirely disentangle the respective heat transport contributions of wind-driven gyre circulations and deep overturning circulations. For example, $\overline{\mathrm{MHT}}_O$ includes both warm shallow wind-driven overturning cells and cold deep overturning cells. Approaches to distinguish the heat transport related to individual meridional overturning cells via a so-called heatfunction were introduced by *Boccaletti et al.* [2005], *Greatbatch and Zhai* [2007], and *Ferrari and Ferreira* [2011] and applied, e.g., by *Yang et al.* [2015]. However, these approaches do not separate the contributions by horizontal circulations which are captured by $\overline{\mathrm{MHT}}_H$ and mainly related to wind-driven circulations. Since we are interested into the changes in MHT due to the reorganization of the wind-driven horizontal circulation in the SO (equatorward expansion of the subpolar gyre system, section 3.1), the decomposition by equations (4) and (5) appears more appropriate for this study. Nevertheless, we encourage the application of other decompositions of MHT (e.g., via the heatfunction approach) in future paleoceanographic studies.

Figure 6 shows both $\overline{\mathrm{MHT}}_O$ (Figure 6b) and $\overline{\mathrm{MHT}}_H$ (Figure 6c) for all simulations. As before we find that the eddying simulations (blue and black curves) generally show larger magnitudes than the corresponding noneddying simulations (red and green curves) both in $\overline{\mathrm{MHT}}_O$ and $\overline{\mathrm{MHT}}_H$. Moreover, the differences in MHT for both *R*0.1 versus *x*1 and DP_{op} versus DP_{cl} have a clear latitudinal separation: Within the tropics differences in MHT are mostly related to meridional overturning circulations (curves of $\overline{\mathrm{MHT}}_H$ largely overlap), whereas in the subpolar regions differences are mostly related to horizontal circulations (curves of $\overline{\mathrm{MHT}}_O$ largely overlap or go to zero).

More precisely, similar to *Volkov et al.* [2010], we find that within the SO for both DP_{op} simulations (black and green curves) the northward $\overline{\mathrm{MHT}}_O$ is exceeded by the southward $\overline{\mathrm{MHT}}_H$, leading to a net southward MHT in the SO. For DP_{cl} (blue and red curves) the $\overline{\mathrm{MHT}}_O$ decreases (remaining northward) whereas the magnitude of $\overline{\mathrm{MHT}}_H$ increases leading to the increased southward MHT in the SO.

The previously noted difference in poleward MHT in the SO between $DP_{op}^{R0.1}$ and DP_{op}^{x1} (section 5.1 and Figure 5a) reappears here mainly in $\overline{\mathrm{MHT}}_H$ and then nearly vanishes for DP_{cl}. Consequently, differences between $DP_{op}^{R0.1}$ and DP_{op}^{x1} in MHT within the SO are mostly related to the barotropic circulation, that is, to different partitionings of the SO flow field into ACC and subpolar gyres (section 3.1 and Figures 1a and 1c).

In other words, the weaker ACC transport in $DP_{op}^{R0.1}$ implies a larger subpolar gyre system in the SO leading to larger poleward MHT compared to DP_{op}^{x1}. For DP_{cl} the partitioning of the subpolar flow field is suspended such that the MHTs for both configurations *x*1 and *R*0.1 are more similar in the SO. Ultimately, the larger change in MHT within the DP_{x1} simulations induces the larger temperature changes at the Antarctic coast (section 4 and Figure 4).

Within the tropics $\overline{MHT}_O$ and $\overline{MHT}_H$ also oppose each other. But here $\overline{MHT}_O$ dominates the MHT and carries the differences between both *R*0.1 versus *x*1 and DP_{op} versus DP_{cl}. We note that in the tropics of the SH the $\overline{MHT}_O$ of DP_{op} (black and green curves) is southward which indicates that the southward MHT by the shallow wind-driven overturning cells exceeds the northward MHT by the deep overturning related to NADW formation. Similarly, we find that in the tropics of the NH the $\overline{MHT}_O$ of DP_{cl} (blue and red curves) is drastically decreased (due to the shutdown of NADW formation) but still northward. That is, the northward MHT by the shallow wind-driven overturning cells exceeds the southward MHT by the deep diffusively driven overturning shown in Figures 2b and 2d. In contrast, around 35°N the $\overline{MHT}_O$ of DP_{cl} indeed becomes southward (i.e., is dominated by deep overturning) and the northward subtropical gyre MHT is mostly present in $\overline{MHT}_H$ (i.e., heat transported horizontally).

Finally, in the northern subpolar region $\overline{MHT}_H$ dominates MHT again (i.e., heat is transported horizontally by the subpolar gyre). However, we note that here the reduction in $\overline{MHT}_H$ due to closing DP is a secondary effect. Namely the strengthening of $\overline{MHT}_H$ in the SO related to the equatorward expansion of the subpolar gyres and the changes in $\overline{MHT}_O$ related to the shutdown of NADW formation are direct consequences of closing DP. In contrast, the northern subpolar gyres are not directly affected by a closed DP, but it is the ceasing heat supply by the deep overturning circulation (seen in $\overline{MHT}_O$) which subsequently leads to a reduced northward MHT by the North Atlantic subpolar gyre.

6. Summary and Discussion

The effects of ocean gateways on the global ocean circulation and climate have been explored with a variety of general circulation models [*Yang et al.*, 2013]. In particular, SO gateways have been investigated due to their possibly crucial role in the onset of Antarctic glaciation during the Eocene-Oligcene transition [*Kennett*, 1977; *Toggweiler and Bjornsson*, 2000; *Sijp et al.*, 2011]. However, all of these models employ low model grid resolutions (larger than 2° horizontally) such that the effects of mesoscale eddies have to be parameterized. In this study, we examined the effects of closing DP within a state-of-the-art high-resolution global ocean model (nominal horizontal resolution of 0.1°) which allows the explicit representation of energetic mesoscale features as well as finer topographic structures. For comparison, we also considered the same model experiments at lower noneddying resolution (nominal 1.0°). The closed DP simulations are configured as sensitivity studies in the sense that the closure of DP is the only change in the ocean bathymetry which is otherwise identical to the present-day control simulation.

The results are twofold: On the one hand, the model behavior on the large scale is qualitatively similar at both resolutions, but on the other hand, the quantitative details significantly depend on the chosen resolution. With respect to the qualitative changes induced by closing DP that are similar at both resolutions we find that the SST significantly increases all around Antarctica with the maximum warming located west of DP. In terms of flow field the subpolar gyres expand equatorward and strengthen whereas the subtropical gyre system is largely unaltered. Moreover, the overturning circulation related to NADW formation shuts down. A detailed analysis of the MHT reveals that the changes in eddy MHT are relatively small such that the changes in MHT are largely dominated by the time mean fields. Furthermore, it turns out that the warming around Antarctica is mostly determined by the changes in the horizontal circulation of the SO, namely, the equatorward expansion of the subpolar gyres which increases the heat transport toward Antarctica. In contrast, the collapse of the MOC related to NADW formation dominates the changes in MHT outside of the SO leading to surface cooling in the North Atlantic.

That both configurations (*x*1 and *R*0.1) show qualitatively similar changes in the large-scale ocean circulation is in accordance with current theories of both the barotropic circulation and the MOC since closing DP profoundly changes the leading-order zonal-momentum balance in the SO. More precisely, closing DP inevitably implies that geostrophy is also zonally established as leading order balance within the latitudes and depths of DP [*Gill and Bryan*, 1971; *Toggweiler and Samuels*, 1995]. Hence, the overall pattern of the closed DP large-scale barotropic circulation can be anticipated from linear theory of the large-scale wind-driven gyre circulation

[*Pedlosky*, 1996; *Huber et al.*, 2004; *Huber and Nof*, 2006]. In particular, the subpolar gyres expand equatorward because the line of zero wind stress curl in the SO is mostly located north of DP (around 50°S).

Moreover, current theories of the overturning circulation divide the MOC into an adiabatic part and a diabatic part [*Kuhlbrodt et al.*, 2007; *Wolfe and Cessi*, 2014], in particular, in the SO [*Marshall and Radko*, 2003; *Olbers and Visbeck*, 2005; *Ito and Marshall*, 2008; *Marshall and Speer*, 2012]. The pole-to-pole circulation of NADW is considered to be largely adiabatic such that NADW leaves the diabatic formation region by sliding adiabatically at depth all the way to the SO, where it is upwelled mechanically along sloping isopycnals by deep-reaching Ekman suction driven by surface westerlies. The necessary ingredients for the adiabatic pole-to-pole cell are a circumpolar channel subjected to surface westerlies, which allows the wind-driven circulation to penetrate to great depth, and a set of isopycnals outcropping in both the channel and the NH [*Wolfe and Cessi*, 2014]. Hence, closing DP is one way (next to closing the "shared isopycnal window") to collapse the adiabatic pole-to-pole cell, as it turns the deep-reaching Ekman suction into shallow gyre Ekman pumping [*Toggweiler and Samuels*, 1995, 1998; *Toggweiler and Bjornsson*, 2000]. On the other hand, weak mixing can support diabatic overturning cells. Mixing and wind forcing near the surface can support diabatic surface cells in the tropics and subtropics; bottom-intensified mixing can support a diffusively driven deep overturning cell associated with bottom water. These types of diffusive overturning cells are what remains of the AMOC in the DP_{cl} configuration at both resolutions.

However, the quantitative details of the ocean circulation (and related heat transports and temperature distributions) are significantly sensitive to ocean modeling details (in contrast to suggestions by *Huber et al.* [2004] and *Huber and Nof* [2006]). Consequently, we find that the warming around Antarctica is substantially larger for the noneddying configuration (~[5.5°C) than for the eddying configuration (~]2.5°C). It turns out that this is a consequence of the subpolar mean flow which partitions differently into gyres and circumpolar current at different resolutions (the DP transport is 159 Sv (119) for $x1$ ($R0.1$)) leading to different heat transports toward Antarctica. In other words, different representations of mesoscale eddies and topographic details (inducing different interactions between mean flow, mesoscale eddies, and topography) do not alter the basic principles of the ocean circulation but can significantly alter quantitative details.

These quantitative details are especially important when it comes to thresholds. For example, sufficient conditions for the onset of a circumpolar current within the SO are still under debate [*Lefebvre et al.*, 2012]. First, it is unclear how deep and/or wide an ocean gateway is required for the development of a significant circumpolar flow. Second, it is under investigation if a DP latitude band uninterrupted by land represents a necessary condition for a strong circumpolar current. Recently, *Munday et al.* [2015] suggested that an open Tasman Seaway is not a necessary prerequisite but that only an open DP is necessary for a substantial circumpolar transport. Support comes from the model simulations of *Sijp et al.* [2011] which show strong circumpolar flow around Australia prior to the opening of the Tasman Seaway and an additional southern circumpolar route when the Tasman Seaway is unblocked. This suggests that Antarctic cooling related to the decrease of the subpolar gyres due to the emergence of circumpolar flow (as seen in this study) could have been at work twice, namely, both when DP opened and subsequently when the Tasman Seaway opened.

Closely related to the inception of a circumpolar current is the partitioning of the resulting subpolar flow field into circumpolar current and subpolar gyre system. As shown in this study, the stronger the resulting circumpolar flow, the smaller the range of latitudes occupied by the subpolar gyres and, consequently, the larger the reduction in poleward heat transport. Hence, this question is closely related to the circumpolar current transport for which it is known that mesoscale eddies and details of continental and bathymetric geometry are crucial [*Rintoul et al.*, 2001; *Olbers et al.*, 2004; *Kuhlbrodt et al.*, 2012; *Hogg and Munday*, 2014], but a robust quantitative theory is still lacking [*Nadeau and Ferrari*, 2015; *Gent et al.*, 2001].

Finally, we note that also the MOC is sensitive to ocean modeling details. This concerns primarily the diffusively driven part of the MOC, as it depends on the mixing coefficients as well as on the numerical diffusion [*Kuhlbrodt et al.*, 2007]. Moreover, as the diffusively driven overturning affects the ocean density distribution it impacts the shared isopycnal window between the SH and the NH [*Wolfe and Cessi*, 2014]. Consequently, the diffusively driven overturning may "precondition" the onset of the adiabatic overturning circulation related to NADW formation [*Borrelli et al.*, 2014].

7. Conclusions and Perspectives

1. From the detailed analysis of meridional heat transports presented in this sensitivity study, we conclude that the ocean gateway mechanism responsible for changes in sea surface temperature (SST) around Antarctica is most likely based on changes in the horizontal ocean circulation. It works as follows (see, e.g., Figures 1a and 1b): The onset of a circumpolar current within the Southern Ocean (e.g., due to gateway opening) leads to a partitioning of the subpolar flow field into a circumpolar current and subpolar gyres which reduces the range of latitudes occupied by as well as the strength of the subpolar gyres. This reduces the subpolar gyre heat transport toward Antarctica and induces cooling near Antarctica. The opposite happens (i.e., equatorward expansion and strengthening of subpolar gyres inducing increased poleward heat transport) if a circumpolar current ceases to exist (e.g., due to gateway closure).
   Since the wind-driven gyres are to first order governed by the fundamental sverdrup balance and both the basic wind patterns (i.e., high and low pressure systems) as well as the south-north SST gradient are inevitable, we expect that the ocean gateway mechanism is robust. That is, we expect it to be qualitatively independent of both the ocean modeling details and the coupling to the atmosphere. What remains is to adequately quantify the changes in SST due to changes in the subpolar ocean circulation and to disentangle these from SST changes induced by other mechanisms like CO_2 increase or ice growth.
2. The quantification of the ocean gateway mechanism relates to several aspects like (i) the sufficient conditions for the onset of a circumpolar current within the Southern Ocean, (ii) the quantitative partitioning of the resulting subpolar flow field into circumpolar current and subpolar gyre system, and (iii) the corresponding changes in meridional heat transports and SST. These aspects are likely highly sensitive to ocean modeling details.
   This concerns the dependence on resolution since different representations of both mesoscale eddies and topographic details can lead to significantly different interactions between mean flow, mesoscale eddies, and topography [*Hogg and Munday*, 2014; *Abernathey and Cessi*, 2014]. Furthermore, this concerns the bathymetric details on their own since paleogeographic reconstructions face substantial uncertainties due to inaccuracies in proxies or plate tectonic reconstructions [*Baatsen et al.*, 2015]. In particular, the exact latitudes of the Southern Ocean ocean gateways (as well as their relative positioning) are uncertain which may substantially effect (i)–(iii). Ideally, one would have to access the uncertainty in the details of continental and bathymetric geometry by considering an ensemble of topographies (reflecting the key uncertainties) in order to estimate the probability distributions of crucial measures like (i)–(iii).
3. Finally, in order to get a detailed picture of the physical processes actually responsible for the changes in heat transport and temperature around Antarctica within the different models of paleoclimatic studies, we suggest more precise attributions of the pathways of heat by decomposing the heat transport into dynamical components, as performed in this study (as well as, e.g., outlined in *Ferrari and Ferreira* [2011] and applied in *Yang et al.* [2015]).
   Moreover, each tracer (e.g., salt, chemical, and organic tracers) follows different pathways in a zonally integrated picture as a result of the different sources and sinks, even though all tracers are transported by the same three-dimensional velocity field [*Ferrari and Ferreira*, 2011; *Viebahn and Eden*, 2012]. Paleoclimatic studies represent a distinguished context to explore the diversity of tracer pathways. Hence, we suggest to perform similar decompositions also for other tracers relevant for Cenozoic climate change like planktic foraminifera [*Sebille et al.*, 2015] or carbon [*Zachos et al.*, 2008; *Ito et al.*, 2004, 2010].

Acknowledgments
The model data used in this paper are available from the corresponding author upon request (j.p.viebahn@uu.nl). This work was funded by the Netherlands Organization for Scientific Research (NWO), Earth and Life Sciences, through project ALW 802.01.024. The computations were done on the Cartesius at SURFsara in Amsterdam. The use of the SURFsara computing facilities was sponsored by NWO under the project SH-209-14.

References

Abernathey, R., and P. Cessi (2014), Topographic enhancement of eddy efficiency in baroclinic equilibration, *J. Phys. Oceanogr.*, *44*, 2107–2126.
Adcock, S. T., and D. P. Marshall (2000), Interactions between geostrophic eddies and the mean circulation over large-scale bottom topography, *J. Phys. Oceanogr.*, *30*, 3223–3238.
Baatsen, M., D. J. J. van Hinsbergen, A. S. von der Heydt, H. A. Dijkstra, A. Sluijs, H. A. Abels, and P. K. Bijl (2015), A generalised approach to reconstructing geographical boundary conditions for palaeoclimate modelling, *Clim. Past Discuss.*, *11*, 4917–4942.
Barnier, B., et al. (2006), Impact of partial steps and momentum advection schemes in a global ocean circulation model at eddy-permitting resolution, *Ocean Dyn.*, *56*, 543–567.
Biastoch, A., J. R. E. Lutjeharms, C. W. Böning, and M. Scheinert (2008), Mesoscale perturbations control inter-ocean exchange south of Africa, *Geophys. Res. Lett.*, *35*, L20602, doi:10.1029/2008GL035132.
Boccaletti, G., R. Ferrari, A. Adcroft, D. Ferreira, and J. C. Marshall (2005), The vertical structure of ocean heat transport, *Geophys. Res. Lett.*, *32*, 1–4, doi:10.1029/2005GL022474.
Borrelli, C., B. S. Cramer, and M. E. Katz (2014), Bipolar Atlantic deepwater circulation in the middle-late Eocene: Effects of Southern Ocean gateway, *Paleoceanography*, *29*, 308–327.
Bryan, F. O., P. R. Gent, and R. Tomas (2014), Can Southern Ocean eddy effects be parameterized in climate models, *J. Clim.*, *27*, 411–425.

Bryan, K. (1996), The role of mesoscale eddies in the poleward transport of heat by the oceans: A review, *Physica D*, *98*, 249–257.
Bryden, H. L. (1979), Poleward heat-flux and conversion of available potential-energy in Drake Passage, *J. Mar. Res.*, *37*, 1–22.
Bryden, H. L., and S. Imawaki (2001), Ocean heat transport, in *Ocean Circulation and Climate*, edited by G. Siedler, J. Church, and J. Gould, pp. 495–474, Academic Press, Elsevier, New York.
Cristini, L., K. Grosfeld, M. Butzin, and G. Lohmann (2012), Influence of the opening of the Drake Passage on the Cenozoic Antarctic Ice Sheet: A modeling approach, *Palaeogeogr. Palaeoclimatol. Palaeoecol.*, *339–341*, 66–73.
DeConto, R. M., and D. Pollard (2003), Rapid Cenozoic glaciation of Antarctica induced by declining atmospheric CO_2, *Nature*, *421*, 245–249.
DeConto, R. M., D. Pollard, and D. Harwood (2007), Sea ice feedback and Cenozoic evolution of Antarctic climate and ice sheets, *Paleoceanography*, *22*, PA3214, doi:10.1029/2006PA001350.
Den Toom, M., H. A. Dijkstra, W. Weijer, M. W. Hecht, M. E. Maltrud, and E. V. Sebille (2014), Response of a strongly eddying global ocean to North Atlantic freshwater perturbations, *J. Phys. Oceanogr.*, *44*, 464–481.
Dewar, W. K. (2002), Baroclinic eddy interaction with isolated topography, *J. Phys. Oceanogr.*, *32*, 2789–2805.
Dijkstra, H. A. (2013), *Nonlinear Climate Dynamics*, Cambridge Univ. Press, New York.
Dukowicz, J. K., and R. D. Smith (1994), Implicit free-surface method for the Bryan-Cox-Semtner ocean model, *J. Geophys. Res.*, *99*, 7991–8014.
Exon, N., et al. (2002), Drilling reveals climatic consequence of Tasmanian Gateway opening, *Eos Trans. AGU*, *83*, 253–259.
Farneti, R., T. L. Delworth, A. J. Rosati, S. M. Griffies, and F. Zeng (2010), The role of mesoscale eddies in the rectification of the Southern Ocean response to climate change, *J. Phys. Oceanogr.*, *40*, 1539–1557.
Farneti, R., and P. R. Gent (2011), The effects of the eddy-induced advection coefficient in a coarse-resolution coupled climate model, *Ocean Modell.*, *39*, 135–145.
Ferrari, R., and D. Ferreira (2011), What processes drive ocean heat transport?, *Ocean Modell.*, *38*, 171–186.
Gent, P. R., and G. Danabasoglu (2011), Response to increasing Southern Hemisphere winds in CCSM4, *J. Clim.*, *24*, 4992–4998.
Gent, P. R., and J. C. McWilliams (1990), Isopycnal mixing in ocean circulation models, *J. Phys. Oceanogr.*, *20*, 150–155.
Gent, P. R., W. G. Large, and F. O. Bryan (2001), What sets the mean transport through Drake Passage?, *J. Geophys. Res.*, *106*, 2693–2712.
Gill, A. E., and K. Bryan (1971), Effects of geometry on the circulation of a three-dimensional southern-hemisphere ocean model, *Deep Sea Res.*, *18*, 685–721.
Goldner, A., N. Herold, and M. Huber (2014), Antarctic glaciation caused ocean circulation changes at the Eocene-Oligocene transition, *Nature*, *511*, 574–577.
Greatbatch, R. J., and X. Zhai (2007), The generalized heat function, *Geophys. Res. Lett.*, *34*, L21601, doi:10.1029/2007GL031427.
Griffies, S. M., et al. (2015), Impacts on ocean heat from transient mesoscale eddies in a hierarchy of climate models, *J. Clim.*, *28*, 952–977.
Hall, M. M., and H. L. Bryden (1982), Direct estimates and mechanisms of ocean heat transport, *Deep Sea Res.*, *29*, 339–359.
Hallberg, B., and A. Gnanadesikan (2006), The role of eddies in determining the structure and response of the wind-driven Southern Hemisphere overturning: Results from the Modeling Eddies in the Southern Ocean (MESO) project, *J. Phys. Oceanogr.*, *36*, 2232–2252.
Hogg, A., and D. R. Munday (2014), Does the sensitivity of Southern Ocean circulation depend upon bathymetric details?, *Philos. Trans. R. Soc. London Ser. A*, *372*, 20130050, doi:10.1098/rsta.2013.0050.
Huber, M., and D. Nof (2006), The ocean circulation in the Southern Hemisphere and its climatic impacts in the Eocene, *Palaeogeogr. Palaeoclimatol. Palaeoecol.*, *231*, 9–28.
Huber, M., H. Brinkhuis, C. E. Stickley, K. Döös, A. Sluijs, J. Warnaar, S. A. Schellenberg, and G. L. Williams (2004), Eocene circulation of the Southern Ocean: Was Antarctica kept warm by subtropical waters?, *Paleoceanography*, *19*, PA4026, doi:10.1029/2004PA001014.
Hurrell, J. W., J. J. Hack, D. Shea, J. M. Caron, and J. Rosinski (2008), A new sea surface temperature and sea ice boundary dataset for the Community Atmosphere Model, *J. Clim.*, *21*, 5145–5153.
Intergovernmental Panel on Climate Change (IPCC) (2013), Summary for policymakers, in *Climate Change 2013: The Physical Science Basis. Contribution of Working Group I to the Fifth Assessment Report of the Intergovernmental Panel on Climate Change*, edited by T. F. Stocker et al., p. 1535, Cambridge Univ. Press, Cambridge, U. K., and New York.
Ito, T., and J. Marshall (2008), Control of lower-limb overturning circulation in the Southern Ocean by diapycnal mixing and mesoscale eddy transfer, *J. Phys. Oceanogr.*, *38*, 2832–2845.
Ito, T., J. Marshall, and M. Follows (2004), What controls the uptake of transient tracers in the Southern Ocean?, *Glob. Biogeochem. Cycles*, *18*, GB2021.
Ito, T., M. Woloszyn, and M. Mazloff (2010), Anthropogenic carbon dioxide transport in the Southern Ocean driven by Ekman flow, *Nature*, *463*, 80–83.
Jayne, S. R., and J. Marotzke (2002), The oceanic eddy heat transport, *J. Phys. Oceanogr.*, *32*, 3328–3345.
Katz, M. E., K. Miller, J. D. Wright, B. S. Wade, J. V. Browning, B. S. Cramer, and Y. Rosenthal (2008), Stepwise transition from the Eocene greenhouse to the Oligocene icehouse, *Nature Geosci.*, *1*, 329–334.
Kennett, J. P. (1977), Cenzoic evolution of Antarctic glaciation, the circum-Antarctic ocean, and their impact on global paleoceanography, *J. Geophys. Res.*, *82*, 3843–3860.
Kirtman, B. P., et al. (2012), Impact of ocean model resolution on CCSM climate simulations, *Clim. Dyn.*, *39*, 1303–1328.
Kuhlbrodt, T., A. Griesel, M. Montoya, A. Levermann, M. Hofmann, and S. Rahmstorf (2007), On the driving processes of the Atlantic meridional overturning circulation, *Rev. Geophys.*, *45*, doi:10.1029/2004RG000166.
Kuhlbrodt, T., R. S. Smith, Z. Wang, and J. M. Gregory (2012), The influence of eddy parameterizations on the transport of the Antarctic Circumpolar Current in coupled climate models, *Ocean Modell.*, *52–53*, 1–8.
Large, W. G., and S. G. Yeager (2004), Diurnal to decadal global forcing for ocean and sea-ice models: the data sets and flux climatologies, *Tech. rep. may, NCAR*, Boulder, Colo.
Le Bars, D., J. V. Durgadoo, H. A. Dijkstra, A. Biastoch, and W. P. M. De Ruijter (2014), An observed 20-year time series of Agulhas leakage, *Ocean Sci.*, *10*, 601–609.
Le Bars, D., J. P. Viebahn, and H. A. Dijkstra (2016), A Southern Ocean mode of multidecadal variability, *Geophys. Res. Lett.*, *43*, 2102–2110, doi:10.1002/2016GL068177.
Lefebvre, V., Y. Donnadieu, P. Sepulchre, D. Swingedouw, and Z.-S. Zhang (2012), Deciphering the role of southern gateways and carbon dioxide on the onset of the Antarctic Circumpolar Current, *Paleoceanography*, *27*, PA4201, doi:10.1029/2012PA002345.
Le Sommer, J., T. Penduff, S. Theetten, G. Madec, and B. Barnier (2009), How momentum advection schemes influence current-topography interactions at eddy permitting resolution, *Ocean Modell.*, *29*, 1–14.
Livermore, R., A. Nankivell, G. Eagles, and P. Morris (2005), Paleogene opening of Drake Passage, *Earth Planet. Sci. Lett.*, *236*, 459–470.
Livermore, R., C. Hillenbrand, M. Meredith, and G. Eagles (2007), Drake Passage and Cenozoic climate: An open and shut case?, *Geochem. Geophys.*, *8*, Q01005, doi:10.1029/2005GC001224.

Macdonald, A. M., and M. O. Baringer (2013), Ocean heat transport, in *Ocean Circulation and Climate, A 21st Century Perspective, Int. Geophys. Ser.*, vol. 103C, edited by G. Siedler et al., Academic Press, Elsevier, Oxford, U. K.
Maltrud, M., and J. L. McClean (2005), An eddy resolving global 1/10 ocean simulation, *Ocean Modell.*, *8*, 31–54.
Maltrud, M., F. Bryan, and S. Peacock (2010), Boundary impulse response functions in a century-long eddying global ocean simulation, *Environ. Fluid Mech.*, *10*, 275–295.
Marshall, J., and T. Radko (2003), Residual-mean solutions for the Antarctic Circumpolar Current and its associated overturning circulation, *J. Phys. Oceanogr.*, *33*, 2341–2354.
Marshall, J., and K. Speer (2012), Closure of the meridional overturning circulation through Southern Ocean upwelling, *Nat. Geosci.*, *5*, 171–180.
Marshall, J., D. Olbers, H. Ross, and D. Wolf-Gladrow (1993), Potential vorticity constraints on the dynamics and hydrography of the Southern Ocean, *J. Phys. Oceanogr.*, *23*, 465–487.
McClean, J. L., et al. (2011), A prototype two-decade fully-coupled fine-resolution CCSM simulation, *Ocean Modell.*, *39*, 10–30.
Meijers, A. J., N. L. Bindoff, and J. L. Roberts (2007), On the total, mean, and eddy heat and freshwater transports in the Southern Hemisphere of a 1/8 × 1/8 global ocean model, *J. Phys. Oceanogr.*, *37*, 277–295.
Mikolajewicz, U., and E. Maier-Reimer (1994), Mixed boundary conditions in ocean general circulation models and their influence on the stability of the model's conveyor belt, *J. Geophys. Res.*, *99*, 633–644.
Mikolajewicz, U., E. Maier-Reimer, T. J. Crowley, and K. Y. Kim (1993), Effect of Drake and Panamanian gateways on the circulation of an ocean model, *Paleoceanography*, *8*, 409–426.
Miller, K. G., J. D. Wright, M. E. Katz, B. S. Wade, J. V. Browning, B. S. Cramer, and Y. Rosenthal (2009), Climate threshold at the Eocene-Oligocene transition: Antarctic ice sheet influence on ocean circulation, in *The Late Eocene Earth-Hothouse, Icehouse, and Impacts*, edited by C. Koeberl and A. Montanari, *Geol. Soc. Am. Spec. Pap.*, *452*, 169–178.
Munday, D. R., H. L. Johnson, and D. P. Marshall (2015), The role of ocean gateways in the dynamics and sensitivity to wind stress of the early Antarctic Circumpolar Current, *Paleoceanography*, *30*, 284–302.
Munk, W. H., and E. Palmen (1951), Note on the dynamics of the Antarctic Circumpolar Current, *Tellus*, *3*, 53–55.
Nadeau, L.-P., and R. Ferrari (2015), The role of closed gyres in setting the zonal transport of the Antarctic Circumpolar Current, *J. Phys. Oceanogr.*, *45*, 1491–1509.
Olbers, D., and V. O. Ivchenko (2001), On the meridional circulation and balance of momentum in the Southern Ocean of POP, *Ocean Dyn.*, *52*, 79–93.
Olbers, D., and M. Visbeck (2005), A zonally averaged model of the meridional overturning in the Southern Ocean, *J. Phys. Oceanogr.*, *35*, 1190–1205.
Olbers, D., D. Borowski, C. Völker, and J.-O. Wölff (2004), The dynamical balance, transport and circulation of the Antarctic Circumpolar Current, *Antarct. Sci.*, *16*, 439–470.
Olbers, D., J. Willebrand, and C. Eden (2012), *Ocean Dynamics*, Springer, Berlin.
Pagani, M., M. Huber, Z. Liu, S. M. Bohaty, J. Henderiks, W. Sijpa, S. Krishnan, and R. M. DeConto (2011), The role of carbon dioxide during the onset of Antarctic glaciation, *Science*, *323*, 1261–1264.
Pedlosky, J. (1996), *Ocean Circulation Theory*, Corrected 2nd printing 1998 of the 1st edition 1996, Springer, Berlin.
Rahmstorf, S., and J. Willebrand (1995), The role of temperature feedback in stabilizing the thermohaline circulation, *J. Phys. Oceanogr.*, *25*, 787–805.
Redi, M. H. (1982), Oceanic isopycnal mixing by coordinate rotation, *J. Phys. Oceanogr.*, *12*, 1154–1158.
Rintoul, S. R., C. W. Hughes, and D. Olbers (2001), The Antarctic Circumpolar Current system, in *Ocean Circulation and Climate*, edited by G. Siedler, J. Church, and J. Gould, pp. 271–302, Academic Press, New York.
Scher, H. D., and E. E. Martin (2006), Timing and climatic consequences of the opening of Drake Passage, *Science*, *312*, 428–430.
Sebille, E., P. Scussolini, J. V. Durgadoo, F. J. C. Peeters, A. Biastoch, W. Weijer, C. Turney, C. B. Paris, and R. Zahn (2015), Ocean currents generate large footprints in marine palaeoclimate proxies, *Nature*, *6*, 6521, doi:10.1038/ncomms7521.
Sijp, W. P., and M. H. England (2004), Effect of the Drake Passage throughflow on global climate, *J. Phys. Oceanogr.*, *34*, 1254–1266.
Sijp, W. P., M. H. England, and J. R. Toggweiler (2009), Effect of ocean gateway changes under greenhouse warmth, *J. Clim.*, *22*, 6639–6652.
Sijp, W. P., M. H. England, and M. Huber (2011), Effect of the deepening of the Tasman Gateway on the global ocean, *Paleoceanography*, *26*, PA4207, doi:10.1029/2011PA002143.
Toggweiler, J. R., and H. Bjornsson (2000), Drake Passage and paleoclimate, *J. Quat. Sci.*, *15*, 319–328.
Toggweiler, J. R., and B. Samuels (1995), Effect of Drake Passage on the global thermohaline circulation, *Deep Sea Res.*, *42*, 477–500.
Toggweiler, J. R., and B. Samuels (1998), On the ocean's large-scale circulation near the limit of no vertical mixing, *J. Phys. Oceanogr.*, *28*, 1832–1852.
Treguier, A. M., M. H. England, S. R. Rintoul, G. Madec, J. L. Sommer, and J.-M. Molines (2007), Southern Ocean overturning across streamlines in an eddying simulation of the Antarctic Circumpolar Current, *Ocean Sci.*, *3*, 491–507.
Viebahn, J., and C. Eden (2010), Towards the impact of eddies on the response of the Southern Ocean to climate change, *Ocean Modell.*, *34*(3-4), 150–165, doi:10.1016/j.ocemod.2010.05.005.
Viebahn, J., and C. Eden (2012), Standing eddies in the meridional overturning circulation, *J. Phys. Oceanogr.*, *42*(9), 1486–1508, doi:10.1175/JPO-D-11-087.1.
Volkov, D. L., T. Lee, and L.-L. Fu (2008), Eddy-induced meridional heat transport in the ocean, *Geophys. Res. Lett.*, *35*, L20601, doi:10.1029/2008GL035490.
Volkov, D. L., L.-L. Fu, and T. Lee (2010), Mechanisms of the meridional heat transport in the Southern Ocean, *Ocean Dyn.*, *60*, 791–801.
Ward, M. L., and A. M. Hogg (2011), Establishment of momentum balance by form stress in a wind-driven channel, *Ocean Modell.*, *40*, 133–146.
Weijer, W., F. Vivier, S. T. Gille, and H. A. Dijkstra (2007), Multiple oscillatory modes of the Argentine Basin. Part I: Statistical analysis, *J. Phys. Oceanogr.*, *37*, 2855–2868.
Weijer, W., M. E. Maltrud, M. W. Hecht, H. A. Dijkstra, and M. A. Kliphuis (2012), Response of the Atlantic Ocean circulation to Greenland Ice Sheet melting in a strongly-eddying ocean model, *Geophys. Res. Lett.*, *39*, L09606, doi:10.1029/2012GL051611.
Wolfe, C. L., and P. Cessi (2014), Salt feedback in the adiabatic overturning circulation, *J. Phys. Oceanogr.*, *44*, 1175–1194.
Wunsch, C. (2010), Towards understanding the paleocean, *Quart. Sci. Rev.*, *29*, 1960–1967.
Yang, H., Q. Li, Q. Wang, Y. Sun, and D. Sun (2015), Decomposing the meridional heat transport in the climate system, *Clim. Dyn.*, *44*(9), 2751–2768, doi:10.1007/s00382-014-2380-5.
Yang, S., E. Galbraith, and J. Palter (2013), Coupled climate impacts of the Drake Passage and the Panama Seaway, *Clim. Dyn.*, *43*(1–2), 37–52, doi:10.1007/s00382-013-1809-6.

Zachos, J. C., G. R. Dickens, and R. E. Zeebe (2008), An early Cenozic perspective on greenhouse warming and carbon-cycle dynamics, *Nature*, *451*, 279–283.

Zachos, J. C., M. Pagani, L. Sloan, E. Thomas, and K. Billups (2001), Trends, rhythms, and aberrations in global climate 65 Ma to present, *Science*, *292*, 600–602.

Zhang, S., R. J. Greatbatch, and C. A. Lin (1993), A reexamination of the polar halocline catastrophe and implications for coupled ocean-atmosphere modeling, *J. Phys. Oceanogr.*, *23*, 287–299.